Int. J. Radiation Oncology Biol. Phys., Vol. 80, No. 4, pp. 1268–1277, 2011

0360-3016/$ - see front matter

ELSEVIER

doi:10.1016/j.ijrobp.2010.10.006

PHYSICS CONTRIBUTION

THREE-DIMENSIONAL DOSE ADDITION OF EXTERNAL BEAM RADIOTHERAPY AND BRACHYTHERAPY FOR OROPHARYNGEAL PATIENTS USING NONRIGID REGISTRATION

Eliana M. Vásquez Osorio, B.Sc., Mischa S. Hoogeman, Ph.D., David N. Teguh, M.D., Abrahim Al-Mamgani, M.D., Inger-Karine K. Kolkman-Deurloo, Ph.D., Luiza Bondar, Ph.D., Peter C. Levendag, M.D., Ph.D., and Ben J. M. Heijmen, Ph.D.

Department of Radiation Oncology, Daniel den Hoed Cancer Center, Erasmus Medical Center, Rotterdam, The Netherlands

Purpose: To develop and evaluate a method for adding dose distributions of combined external beam radiotherapy (EBRT) and brachytherapy (BT) for oropharyngeal patients.

Methods and Materials: Two computed tomography (CT) scans were used for 5 patients: the EBRT CT, used for EBRT planning, and the BT CT, acquired after catheter implantation. For each scan, the salivary glands and the chewing and swallowing muscles were contoured, and a dose distribution was calculated. A nonrigid transformation was obtained by registering the organs' surfaces. Then the BT dose distribution was mapped onto the EBRT dose distribution by applying the transformation obtained. To account for differences in fractionation, the physical doses were converted to equivalent dose in 2 Gy (EQD_2), and the total dose was found by adding dose voxel by voxel. The robustness of the dose addition was investigated by varying delineations and input parameters of the registration method and by varying the α/β parameter for EQD_2. The effect of the perturbations was quantified using dose–volume histograms (DVH) and gamma analyses (distance-to-agreement/dose-difference = 1 mm/1 Gy).

Results: The variations in input parameters and delineations caused only small perturbations in the DVH of the added dose distributions. For most organs the gamma index was low, and it was moderately elevated for organs lying in areas with a steep gradient (median gamma index $\leq$2.3 for constrictor muscles, $\leq$0.7 for all other organs).

Conclusions: The presented method allows adding dose distributions of combined EBRT and BT for oropharyngeal patients. In general, the method is reliable and robust with respect to uncertainties in organ delineation, perturbations in input parameters of the method, and α/β values.

Three-dimensional dose addition, Nonrigid registration, Head and neck, Brachytherapy.

INTRODUCTION

A combination of external beam radiotherapy (EBRT) and brachytherapy (BT) is commonly used in the treatment of head-and-neck cancer, cervical cancer, and prostate cancer (1–3). EBRT aims at treating the primary tumor and areas at risk for microscopic disease, whereas BT is used to boost the primary tumor. However, in current clinical practice, BT boosts are optimized independently, and the dose already delivered is not accounted for. The reason is that the addition of three-dimensional (3D) dose distributions is challenging because of anatomic changes in the patient caused, for instance, by weight loss, tumor shrinkage, different patient setups, implantation of catheters, insertion of applicators, or surgical procedures (Fig. 1). Furthermore, to establish dose–effect relationships for tumor control and side effects in combined modality treatments, simple approximations to add dose are often used (4, 5). Some studies use only the EBRT dose to establish dose–effect relationships (4). In other studies, the accumulated dose was approximated without taking patient deformations into account. For example, Teguh *et al.* (5) related the probability of dysphagia to the dose to the swallowing muscles, where the total dose was found by simply adding the physical EBRT and BT mean doses.

Rigid registration, including rotation and translation, followed by the linear addition of the dose matrices, is not accurate to add dose. A rigid transformation does not align deforming anatomy adequately (Fig. 1). Nonrigid registration, on the other hand, allows better alignment of the anatomy, enabling different dose distributions to be mapped to a common frame of reference. Additionally, different modalities often use different fractionation schemes. Therefore,

Reprint requests to: Eliana M. Vásquez Osorio, B.Sc., Erasmus Medical Center - Daniel den Hoed Cancer Center, Department of Radiation Oncology, Groene Hilledijk 301, 3075 EA Rotterdam, The Netherlands. Tel: (+31)10-7041491; Fax: (+31)10-7041012; E-mail: e.vasquezosorio@erasmusmc.nl

Conflict of interest: none.

Acknowledgment—The authors thank Dick Sipkema and Hans Joosten for their technical contributions for this study.

Received March 16, 2010, and in revised form Sept 30, 2010. Accepted for publication Oct 2, 2010.

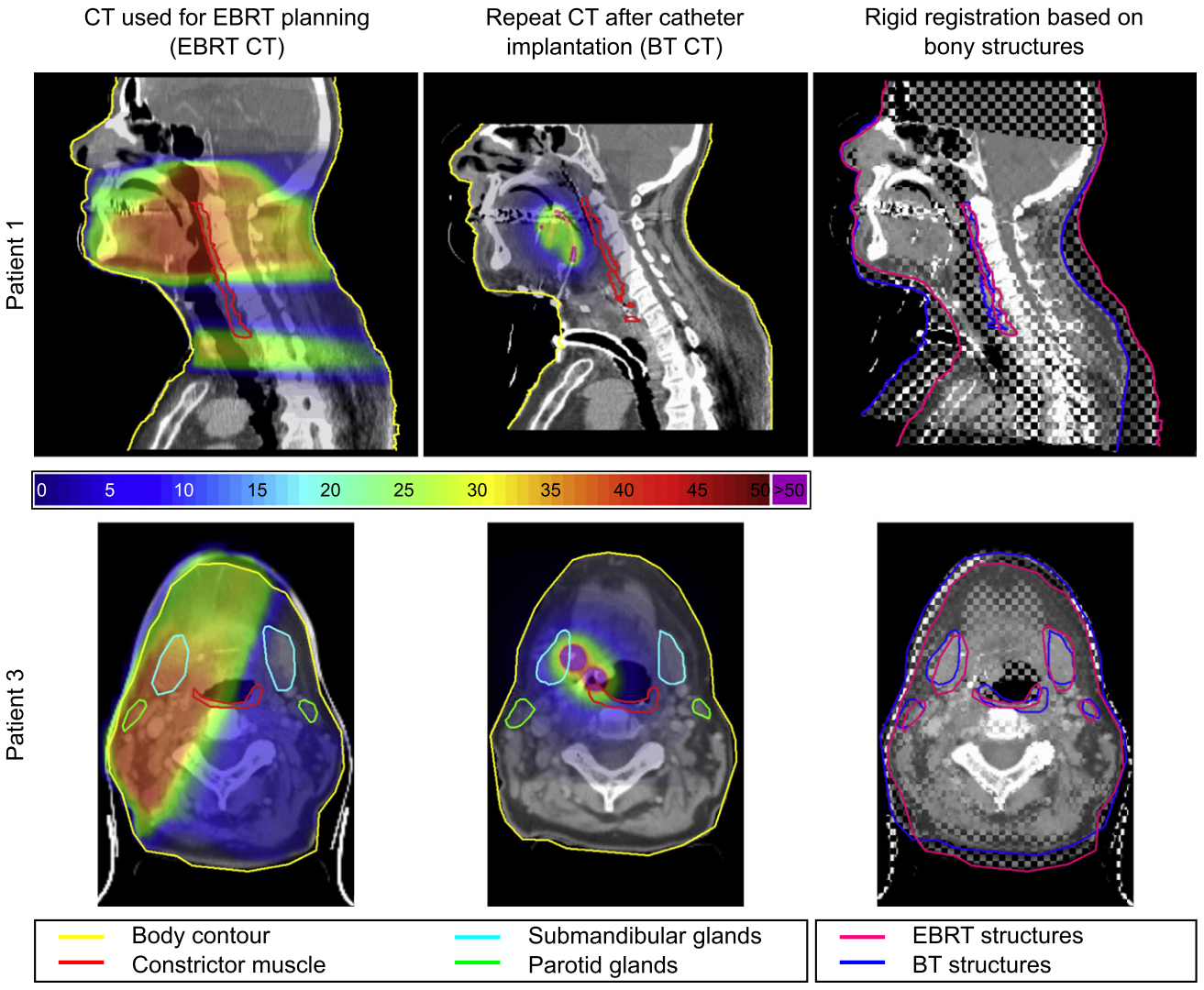

Fig. 1. Anatomic changes between external beam radiotherapy (EBRT) and brachytherapy (BT) for 2 patients. First row, sagittal planes of Patient 1. Notice the large anatomic changes between the EBRT and BT computed tomography (CT) scan, mostly caused by neck dissection, catheter insertion, and different patient positioning. Second row, axial planes of Patient 3. Notice that rigid registration (last column) is not adequate to align both CT scans.

dose distributions require a conversion to biologic equivalent doses before adding the dose in each voxel (6).

In this article we propose a method for adding 3D EBRT and BT dose distributions, using a nonrigid registration framework developed in house, based on Chui *et al.* (7) and previously described in Vásquez Osorio *et al.* (8), and Bondar *et al.* (9). To account for the biologic effects of the different fractionation schemes, the physical dose distributions were converted to the biologic equivalent dose for 2-Gy fractions (EQD_2, (6)) before adding each dose voxel. The method was tested for the organs at risk of 5 oropharyngeal cancer patients treated with EBRT, followed by BT boost (1, 5). The robustness of the dose addition was investigated by variations in input parameters of the registration method, simulating variations in organ delineations around the clinical contours, and by varying the α/β value used for EQD_2.

METHODS AND MATERIALS

Patient data

Five oropharyngeal cancer patients were included in this study (Table 1). These patients belonged to a larger group previously used for quantifying anatomic changes using nonrigid registration (10). According to the protocol (1, 5), the patients first underwent EBRT to a total dose of 46 Gy in 23 fractions (dynamic intensity-modulated RT), followed by a BT boost 2 weeks after the end of EBRT (Pulsed dose-rate BT scheme 2 Gy + 18 × 1 Gy + 2 Gy, biologically equivalent to high dose-rate BT scheme 4 Gy + 4 × 3 Gy + 4 Gy (11)). node-positive patients underwent neck dissection before catheter implantation.

Two intravenous contrast-enhanced computed tomography (CT) scans were used for each patient: the CT scan used for planning EBRT (EBRT CT scan), and a repeat CT scan taken 2 weeks after EBRT, after catheter implantation, and just before BT dose delivery (BT CT scan). The slice spacings were 3 mm and 1.5 mm for the EBRT and BT scans, respectively. The catheters were clearly

Table 1. Patient characteristics

Patient	Sex	Age (y)	Site	TNM staging		
1*†	M	57	Base of tongue	T3	N2a	M0
2‡	M	48	Tonsillar fossa	T2	N0	M0
3‡	F	59	Soft palate	T2	N0	M0
4*†§	M	58	Base of tongue	T3	N2a	M0
5*†	F	52	Base of tongue	T1	N2c	M0

* Both necks treated by external beam radiotherapy.
† Patient underwent neck dissection, where, among other soft tissues, the submandibular glands were removed.
‡ Ipsilateral neck treated by external beam radiotherapy.
§ Patient underwent concomitant chemotherapy.

visible in the BT CT because copper wires were inserted before acquisition. The body contour, chewing muscles (masseter, pterygoid, and temporalis muscles), swallowing muscles (superior, middle and inferior constrictor, cricopharyngeus, and esophagus inlet muscles), and major salivary glands (parotid and submandibular glands) were contoured in both CT scans. For consistency, the BT organs were delineated, using the EBRT contours as reference. All delineations were checked by a second observer. Surfaces, defined by sets of triangles joining contours in consecutive slices, were created from the delineated structures.

Dose distributions for EBRT and BT were calculated using the treatment planning system used clinically at the time: CadPlan v6.4.7 (Varian Medical Systems, USA) and Plato BPS v14.2 (Nucletron, The Netherlands), respectively. The BT dose distribution was originally calculated based on implant reconstruction from orthogonal radiographs. Here, we reconstructed the BT dose distribution on the BT CT scan. Using the catheters in the BT CT scan, the implant geometry and active dwell positions were determined. The dwell times were copied from the original plan. Finally, the BT dose was calculated and the dose grid was exported. Both dose distributions were interpolated to a regular grid ($1 \times 1 \times 1$ mm^3).

Dose addition

Fig. 2 illustrates the steps to add the EBRT and BT dose distributions. First, the triangulated surfaces generated from the delineated structures were used to compute a nonrigid transformation using a nonrigid registration method developed in house (8, 9). The nonrigid registration framework was previously validated using anatomic landmarks (8) and was improved to reinforce inverse consistency (9). The nonrigid transformation, modeled by a regularized thin-plate spline (7), implicitly comprises the changes between the two structure sets by generating a smooth spatial mapping, which is constrained by points lying on the organs' surface. Second, we computed the transformed BT dose by inverse mapping using the Insight Toolkit (12). Inverse mapping finds the transformed BT dose in the grid positions of the EBRT dose by transforming each grid position into the BT dose grid using the spatial mapping defined by the EBRT to BT transformation. Then the dose is interpolated at the mapped location using the dose of the closest neighboring BT grid points. Finally, the interpolated value is stored in the EBRT grid position. This procedure avoids the creation of empty areas in the transformed dose. Third, the physical doses were converted into EQD_2 using the linear quadratic model. Finally, the 3D total dose distribution was calculated by adding the converted EBRT dose and the transformed and converted BT dose voxel by voxel.

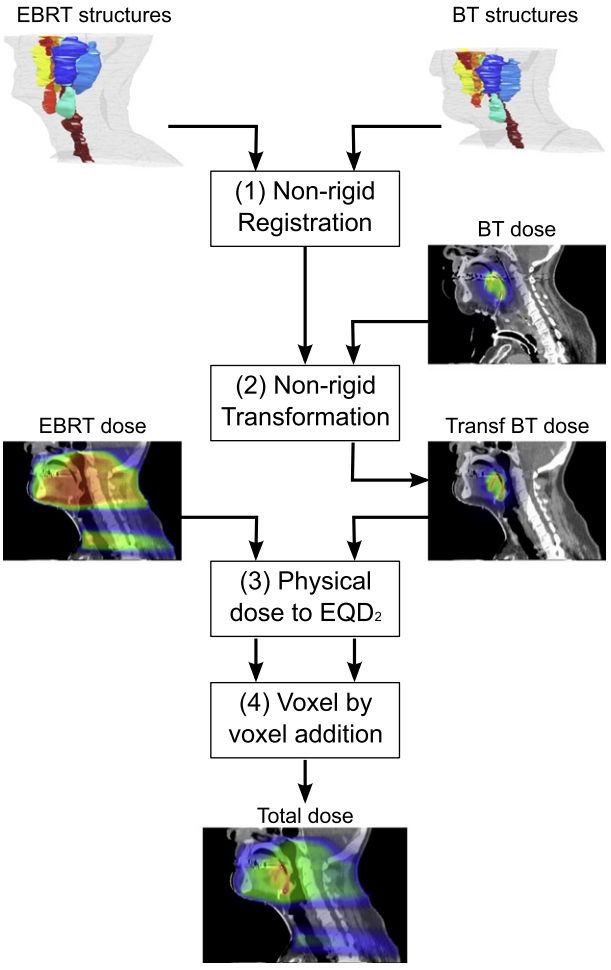

Fig. 2. Schematic showing the steps for dose addition. BT = brachytherapy; EBRT = external beam radiotherapy; EQD_2 = equivalent dose in 2 Gy.

Simple alternatives to full 3D nonrigid registration

We investigated the validity of approximating the D_1, mean dose and D_{99} by adding the separate values for the EBRT and BT dose distributions without taking anatomic changes into account. We defined D_1 and D_{99} as the dose received by the 1% and 99% of the organ's voxels, respectively as read from the DVH data. The approximations were converted to EQD_2 and then compared to the values obtained by nonrigid registration.

Robustness of dose addition

As in previous studies (8), each registration produced a nonrigid transformation, which aligned the surfaces nicely. This was checked by visual inspection and by assuring that the transformation error, defined as the mean distance between surfaces, was below 1 mm. Previously, we validated the anatomic correspondence of the nonrigid registration framework using identifiable landmarks in CT datasets (8). The image sets currently used do not contain sufficient information to indistinguishably identify corresponding tissue elements on a functional subunit level. Alternatively, we investigated the robustness of the dose addition method with respect to changes in (1) the parameters of the nonrigid registration framework, (2) control point distribution, (3) organ delineation, and (4) α/β value used for EQD_2. To assess the influence of these perturbations, we compared each total dose distribution resulting

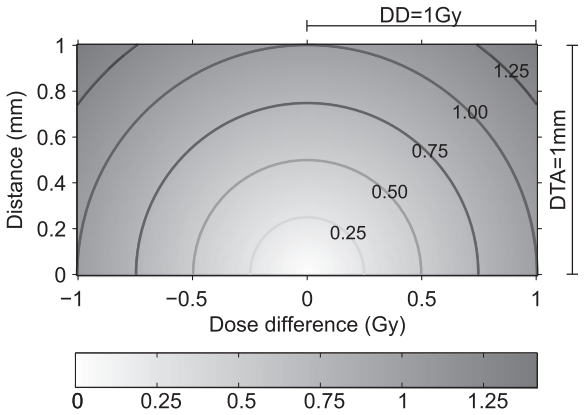

Fig. 3. Gamma index 1mm\1 Gy as a function of distance and dose difference between two voxels. Perfect agreement scores zero (same dose and same spatial position). Two voxels with the same dose in locations separated by a distance of DTA, or with the same spatial position and dose difference of DD, score a gamma index equal to one.

from each perturbation to a reference total dose distribution using dose-volume histograms (DVH) and the gamma index method (13). The reference total dose distribution was calculated using the clinical delineations and reference parameters (r = 5 mm, λ = 5, and α/β = 3 Gy). The gamma index combines the dose-difference (DD) and distance-to-agreement (DTA) to compare two dose distributions (Fig. 3). Gamma index (DTA\DD = 1 mm\1 Gy) was evaluated in each voxel within the delineated structures. We performed a total of 23 perturbations (see below for details) for each of the 5 patients, including 15 organs per patient, which resulted in 1,725 gamma index distributions. We summarized the distributions of gamma indices in box-and-whisker diagrams and reported the percentage of voxels passing the criteria (gamma index $\leq$1).

Perturbations of framework parameters. The nonrigid registration framework uses points to represent the structures to be registered. The framework includes a procedure to generate points from surfaces that is controlled by the density radius r. The parameter r determines the density of control points, which affects the computational time and accuracy. Small r means large number of points, longer computational time, and, theoretically, more accurate results. Conversely, large r produces few points, shorter computational time, and less accurate results. Based on previous experience, we tested r = 5, 6, and 8 mm. The second framework parameter is λ. This weight parameter controls the degree of deformation of the transformation function by regulating the thin-plate spline used as transformation. Large λ restricts the transformation to be mostly affine, opposite to a small λ, which relaxes the restriction. We tested λ = 0.5 and 5, which in combination with the used rs (above) produced transformation errors below 1 mm as in Vásquez Osorio *et al.* (8).

Perturbations in control point distribution. We investigated the influence of using different control point distributions. As mentioned, the framework includes a procedure to generate control points, which spread pseudohomogeneously on the surfaces of the delineated structures (8, 9). In this procedure, a refined surface of the structures is generated by dividing iteratively the triangles that join the contours of consecutive slices. Then, the vertices of the refined triangles are grouped in spheres whose radius is the density radius (r), and the centroid is calculated. Last, the points are replaced by the closest point on the surface to the calculated centroid. By randomly varying the position of the grouping spheres, we generated four control point distributions using r = 6 mm.

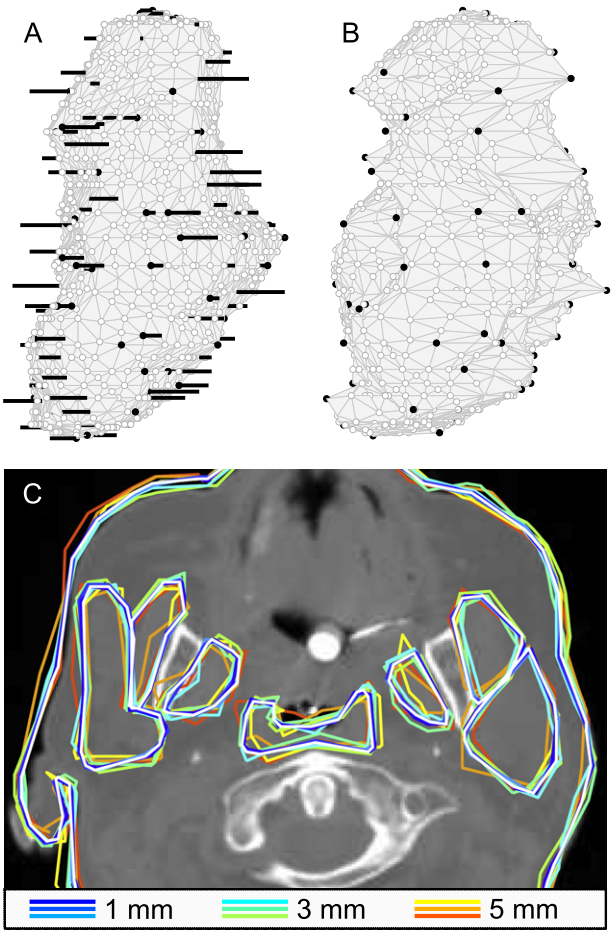

Fig. 4. Procedure to simulate delineation variations. (A) A set of points is randomly selected (black dots) from the points in the original structure (light triangles). Then deforming vectors, restricted to the axial planes, are generated (thick lines), limiting their lengths to the delineation variation simulated (1, 3, or 5 mm). (B) The deformation is interpolated to the rest of the structure using a nonregularized thin-plate spline. (C) Brachytherapy computed tomography scan of Patient 5 showing all nine delineation variations simulated. The clinical delineation is shown in white.

Perturbations in structures delineations. To determine the influence of delineation variations on the nonrigid registration, and consequently on the dose addition, we simulated observer variations of 1, 3, and 5 mm in the delineation of structures. To simulate the variations, random deformations were applied to the surfaces of the EBRT and BT structures (Fig. 4). First, one third of the contour points that constitute the structures' surface was randomly selected. Only points that were not in close proximity to other organs were considered, to avoid overlapping of perturbed contours of neighboring organs. Second, random deformation vectors were generated. To simulate the real situation, the deformation vectors were limited to the axial planes where the contours were drawn, and their direction and length was random, to a maximum of the variation simulated (1, 3, or 5 mm). Third, the deformation was interpolated to the rest of the structure points using a nonregularized thin-plate spline (14). Finally, the deformed structures were used in the nonrigid registration framework to generate the nonrigid transformation. We calculated a total of nine nonrigid

Table 2. EBRT and BT mean doses for each patient and organ

Organ	EBRT; BT mean doses (physical doses, Gy)				
	Patient 1	Patient 2	Patient 3	Patient 4	Patient 5
Left parotid	23.7; 1.4	6.4; 0.8	11.4; 0.8	26.1; 2.5	19.4; 1.7
Right parotid	25.3; 1.4	29.5; 1.5	29.1; 1.6	35.3; 2.3	10.9; 1.5
Left submandibular	47.8; 3.2	2.5; 1.6	5.4; 1.9	44.8; 9.7	46.5; 9.0
Right submandibular	48.7; 4.6	45.3; 4.9	43.6; 9.6	45.8; 20.7	46.4; 6.7
Left masseter	27.1; 2.4	0.7; 0.9	5.4; 0.8	17.6; 2.0	12.8; 2.7
Right masseter	28.5; 2.5	11.4; 2.0	12.8; 2.0	23.7; 2.0	14.8; 2.0
Left pterygoid	31.1; 3.2	2.3; 1.7	12.3; 1.4	25.6; 2.6	13.4; 3.8
Right pterygoid	36.8; 3.3	16.1; 3.2	26.9; 3.7	39.9; 2.4	12.7; 3.4
Left temporalis	18.0; 2.0	0.5; 1.0	2.8; 0.8	20.4; 1.5	1.3; 1.8
Right temporalis	17.1; 1.9	2.3; 1.6	3.0; 1.6	21.5; 1.4	1.3; 1.7
Superior constrictor	47.3; 6.6	26.7; 7.0	33.5; 10.6	44.3; 8.8	45.7; 6.3
Middle constrictor	47.4; 4.3	21.4; 4.6	20.3; 4.7	44.7; 11.6	46.7; 4.3
Inferior constrictor	25.1; 2.5	12.3; 1.9	18.5; 1.7	42.4; 6.5	38.5; 3.4
Cricopharyngeus	17.5; 1.3	10.1; 0.8	17.3; 0.8	41.6; 2.5	29.2; 1.8
Esophagus inlet	20.1; 0.7	7.4; 0.4	16.1; 0.6	39.8; 1.2	30.7; 1.2

Abbreviations: EBRT = external beam radiotherapy; BT = brachytherapy.

transformations per patient, using three random deformations per simulated maximum variation of 1, 3, and 5 mm. Calculation of DVHs and gamma analyses were performed using the nonperturbed delineations to assess only the effects of the perturbations on the results of the dose addition.

Perturbations in α/β values. EQD_2 was used to account for differences in the fractionation schemes for EBRT and BT. EQD_2 is based on the linear-quadratic model, and it uses the biologic parameter α/β (15). The α/β value represents the ratio between the radiosensitivity and the repair capacity of a specified tissue. A common value for late reactions is 3 Gy, but the precise value is uncertain. We investigated the effect of different α/β values on the dose addition by varying α/β by $\pm$20% and $\pm$10% around the reference 3 Gy. We used the nonrigid transformation applied to calculate the reference total dose distribution to assess only the effects of α/β variation.

RESULTS

Total dose

Table 2 summarizes the mean doses per organ and patient for EBRT and BT dose distributions. For all patients, the largest contribution to the total dose came from the EBRT, and most organs at risk received low BT doses. Steep gradients were present in the BT dose distribution, especially within the constrictor muscles (up to 29, 88, and 22 Gy/mm for Patients 2, 3, and 4 respectively). The gradients were caused by the closeness of implanted catheters to the muscles (Fig. 1). Fig. 5 shows the DVHs for the total dose distributions. The largest total doses were found for the constrictor muscles for Patients 3 and 4, and for the right submandibular gland for Patient 3.

We summarized the differences between calculating D_1, the mean dose, and D_{99}, taking anatomic changes into account and ignoring anatomic changes in Table 3. None of the DVH parameters were systematically underestimated or overestimated by the approximation, but large differences were found for D_1.

Perturbations analysis

Besides the DVHs for the reference total dose distributions, Fig. 5 also shows the total dose DVHs for the 23 perturbations. Most perturbations produced only minor deviations with respect to the reference DVHs, to the point at which most total dose DVHs blend into one single curve. The largest variations were found for the middle and inferior constrictor muscles for Patient 4 (framework parameters perturbation $\lambda = 0.5$), the right submandibular glands for Patient 3 (delineation variations of 5 mm), and the pterygoid, and temporalis muscles for the α/β perturbations.

Figs. 6 and 7 summarizes the distributions of gamma indices of all voxels of all organs and patients (>21 million voxels) using box-and-whisker diagrams categorizing the data by perturbation type and by organ per patient, respectively. The perturbations in the control point distributions produced the lowest gamma indices. The largest gamma indices were found for α/β = 2.4 Gy, perturbations using λ = 0.5 and delineation variations of 5 mm (medians and boxes in Fig. 6). The results varied among patients. Patient 4 presented the largest variations and Patient 1 the smallest; and both were base of tongue cases. All chewing muscles, the parotid glands, the esophagus inlet, and the cricopharyngeus muscles presented small gamma indices for all patients. The organs that presented the most variation were the constrictor muscles and the submandibular glands. Similar results were found when each perturbation was independently analyzed (total, 1,725 medians; data not shown). The largest gamma indices were found for the middle and inferior constrictor muscle for Patient 4, framework parameters r = 5, λ = 0.5 (medians up to 2.3 and 2.2). For the rest of the organs for all perturbations and patients, the median was below 0.7.

Table 4 summarizes the voxels passing the strict criteria of the gamma analyses. Most organs scored high values. The lowest values were found for the constrictor muscles using λ = 0.5 and delineation variation of 5 mm, which is in accordance with the data shown in Figs. 6 and 7.

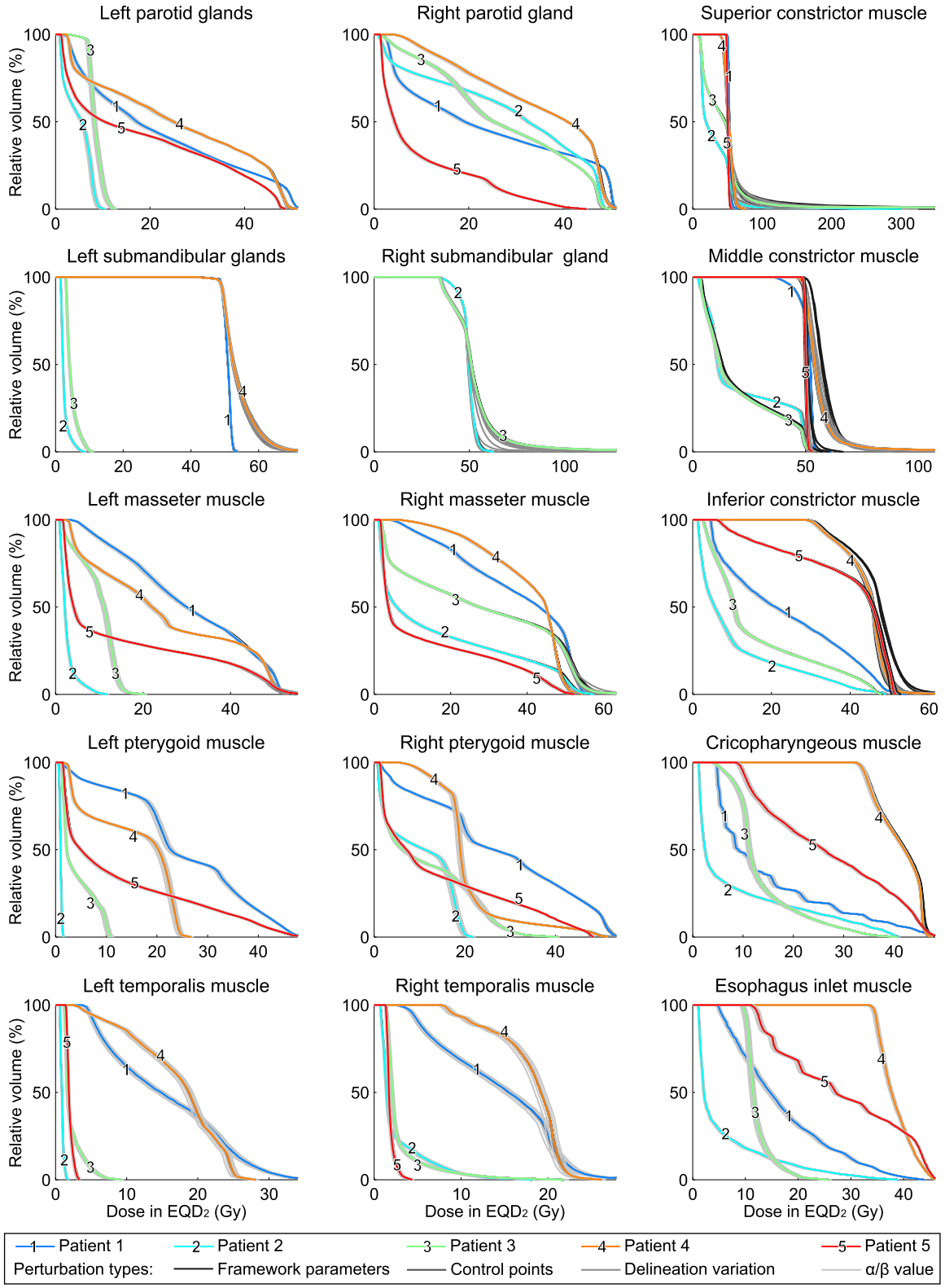

Fig. 5. Dose–volume histograms for the total dose distributions (reference and 23 perturbations). Perturbations on the total dose are shown in different shades of gray, and most of them blend with the reference dose–volume histogram curve. Dose axes were cropped to the largest D_1. EQD_2 = equivalent dose in 2 Gy.

DISCUSSION

We presented a method for adding dose distributions of different modalities, taking into account anatomic changes and biologic effects. The method was applied to the organs at risk of 5 patients with oropharyngeal cancer. A robustness analysis was presented as an alternative to validation against

Table 3. Differences between approximated D_1, mean dose and D_{99} and D_1, mean dose, and D_{99} calculated using nonrigid registration

	Differences (EQD_2,* Gy)	
DVH parameter	Average	Range
D_1	−0.9	−14.5 to 25.6†
Mean dose	−0.1	−2.6 to 0.4
D_{99}	0.1	−1.7 to 1.5

Abbreviation: DVH = dose–volume histogram.
* Using α/β = 3 Gy.
† Maximum D_1 occurred in middle constrictor muscle for Patient 3, shown in lower row in Fig. 1.

ground truth. Overall, the method was robust against perturbations of the input parameters and delineation variations, as demonstrated by the overlapping total dose DVH curves in Fig. 5. Robustness was also investigated by gamma analyses (Figs. 6 and 7), comparing perturbed and reference dose distributions using strict criteria (*i.e.,* 1 mm\1 Gy).

Comparing the perturbation types (medians and boxes in Fig. 6), larger gamma indices were found for α/β variations, $\lambda = 0.5$, and the largest delineation variations (5 mm). The λ parameter controls the flexibility of the transformation, and a low λ produces a more flexible transformation. Compared to the reference dose distributions, total doses calculated by transformations using $\lambda = 0.5$ showed larger local differences, resulting in larger gamma indices (whiskers in Fig. 6). The gamma indices were low for the perturbations in control point distributions, $\lambda = 5$, and delineation variations below 5 mm. Table 4 shows similar results for the percentage of voxels passing the gamma criteria, except for the α/β parameter. Although α/β perturbations produced the largest medians and boxes in Figs. 5 and 6, they scored 100% of voxels passing the gamma criteria. An explanation is that the α/β perturbation affected the whole dose distribution, but the change was below the criteria used for the gamma analyses (1 mm\1 Gy). For the organs studied, the variations caused by the α/β perturbations in the total dose distributions were small (below 1 Gy around 1 mm) and could be seen as clinically not relevant. However, the variations may become greater when adding doses of larger magnitude because of the quadratic form of EQD_2.

Large variations were found in the constrictor muscles and some submandibular glands (Figs. 5 and 7). These organs were close to the target volume, to the extreme that some catheters run shortly along the swallowing muscles, causing a very steep BT dose gradients within these muscles: up to 29, 88, and 22 Gy/mm for Patients 2, 3, and 4 respectively. The location of these organs explains the enhanced effect of the perturbations, especially for those where local differences were present (framework parameters and delineation variations), because even small changes in these areas with steep gradients result in very large variations. A possibility for improving the dose addition in areas with steep gradients is to use a different interpolation method for mapping the BT dose (Fig. 2,

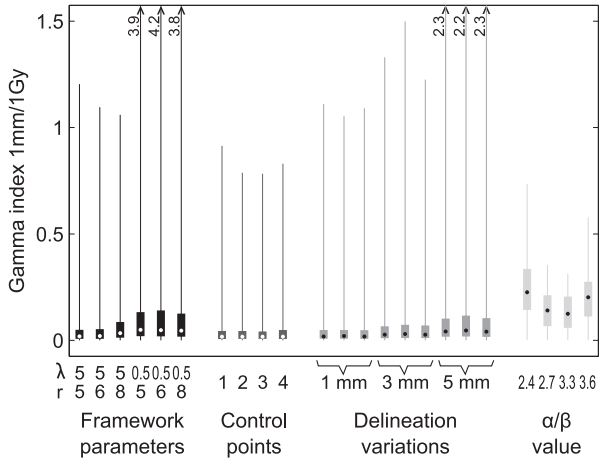

Fig. 6. Distributions of gamma indices 1 mm\1 Gy categorized by perturbation type. The dots represent the median; the boxes extend between the 25th and 75th percentiles and the whiskers between the 0.1 and 99.9 percentiles for all voxels of all organs and patients. Whiskers extending beyond the axis are marked with ^ and their 99.9 percentile is shown next to them.

step 2) for instance octant interpolation as proposed by Rosu *et al.* (16). The concept of accumulating dose using nonrigid registration has been explored in the literature. However, to our knowledge, there has been no previous attempt to add 3D dose distributions of EBRT and BT taking anatomic changes into account. Few reports are available that address the anatomic validity of dose addition. Schaly *et al.* (17) proposed tracking of tissue elements (voxels) between daily CT scans and accumulation of their dose distributions using thin-plate spline. In a sensitivity analysis of control point placement, they found dose differences up to 37% for bladder and 27% for rectum. An alternative approach for dose accumulation uses finite element analysis (18). However, inclusion of anatomic landmarks inside or outside the surfaces is limited, and the mechanical properties for the tissue should be accurate (19).

With respect to the current study, our nonrigid registration method was previously validated using anatomic landmarks (8). Recently Zhong *et al.* (20) suggested that using landmark-based evaluation of nonrigid registrations may potentially underestimate registration errors, because large errors can be made in areas with few anatomic features (areas of relatively uniform intensity). In their study, they created a displacement vector field to create phantoms that were registered. The vector field was then used as a ground truth to compare registration results. In clinical practice (*e.g.,* in our study), such artificial displacement fields are not available for real patient data, and the validation still depends on visual anatomic landmarks. It has been shown in the literature that the registration error increases as its distance from the boundary of organs increases (19, 20). However, the organs analyzed in the current study are small or narrow; therefore, most points are relatively close to the boundary.

The validation for the cases of head-and-neck cancer in Vásquez Osorio *et al.* (8) used points representing the top

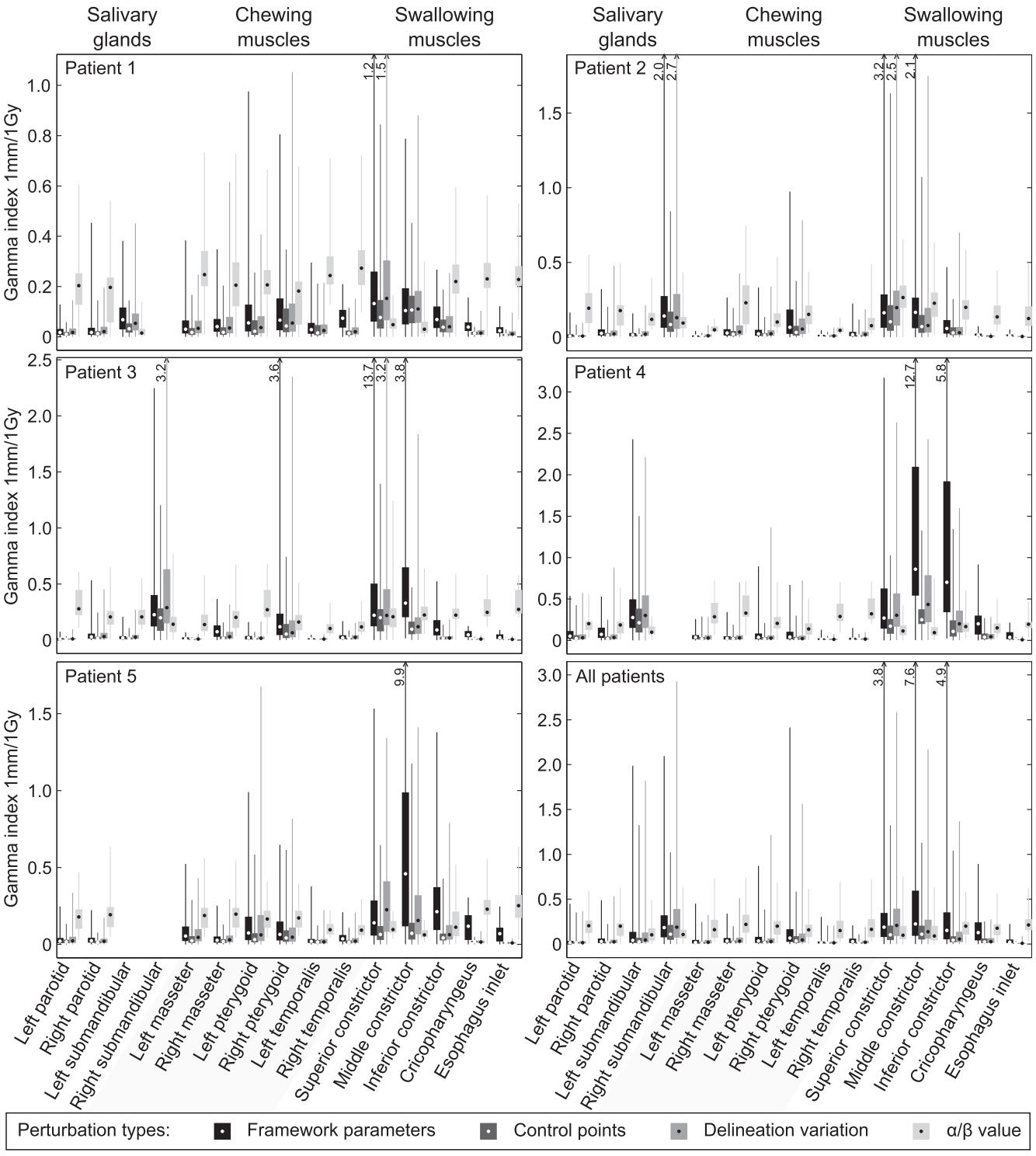

Fig. 7. Distributions of gamma indices 1 mm\1 Gy categorized by organs and perturbation type per patient. See Fig. 6 for information about the diagram.

and bottom of the glands and lines representing the mandible–parotid gland and styloid process—parotid gland interfaces. These lines lay on the surface, and the points were close to the glands' surfaces. Therefore, it can be argued that for cases of head-and-neck cancer, no validation has been made for points inside the organs. On the other hand, the method was validated for larger organs using internal landmarks (cervix and prostate). Moreover, it has been shown that the results of the method can be improved by incorporating additional anatomic information in the nonrigid registration, such as internal anatomic landmarks, represented by lines or points. As an alternative to anatomic validation, in the current study we investigated the robustness of the dose addition method. To further validate the method and

Table 4. Percentage of voxels passing the strict gamma criteria (1mm\1 Gy) for all patients, categorized by perturbation type

	Average(standard deviation) of percentage of voxels that gamma index (1 mm\1 Gy) ≤1 (in %)						
	Framework parameters		Control	Delineation variation			
Organ	λ = 5*	λ = 0.5*	points†	1 mm‡	3 mm‡	5 mm‡	α/β value§
Submandibular glands							
Left	99.4 (1.7)	97.7 (4.2)	99.6 (1.1)	99.5 (1.9)	99.2 (2.3)	96.2 (7.3)	100.0 (0.0)
Right	99.2 (1.7)	94.2 (3.5)	99.8 (0.4)	99.0 (1.7)	92.2 (9.3)	85.3 (12.1)	100.0 (0.0)
Pterygoid muscle							
Left	100.0 (0.0)	99.9 (0.2)	100.0 (0.0)	100.0 (0.0)	100.0 (0.1)	99.5 (0.9)	100.0 (0.0)
Right	100.0 (0.1)	98.8 (2.3)	100.0 (0.0)	100.0 (0.0)	99.7 (0.7)	99.2 (2.4)	100.0 (0.0)
Constrictor muscle							
Superior	99.0 (2.1)	88.9 (11.2)	99.6 (0.9)	99.0 (1.6)	96.2 (3.7)	89.4 (10.7)	100.0 (0.1)
Middle	98.0 (5.3)	69.3 (31.3)	99.8 (0.5)	98.3 (5.4)	99.3 (2.5)	89.6 (14.9)	100.0 (0.0)
Inferior	98.9 (2.4)	84.5 (29.3)	99.9 (0.4)	99.4 (1.5)	99.8 (0.7)	99.3 (1.8)	100.0 (0.0)

Organs not shown scored 100(0.0) in all perturbations.
* Columns combine r = 5, 6, and 8 mm.
† Column combine 4 perturbations.
‡ Columns combine 3 perturbations.
§ Column combine α/β = 2.4, 2.7, 3.3, and 3.6 Gy.

to produce more accurate results, images with better soft-tissue contrast, such as magnetic resonance imaging scans, could be used. However, it should always be considered that dose addition is an approximation of the true dose accumulation, and that the accuracy of the method should be taken into account when applying it in clinical practice.

In the present study, the total dose to the tumor was not calculated. Besides the large changes happening to the target volume because of catheter implantation, several studies have found that target volumes shrink during EBRT treatment (21). Dose accumulation for a regressing mass requires further research to handle disappearing tissue properly.

Table 3 compiles the differences between approximated D_1, mean dose, and D_{99} (by adding the separate values for EBRT and BT) and D_1, mean dose, and D_{99} using nonrigid registration. Large differences were found for D_1 (≤25.6 Gy). The differences were smaller for mean dose and D_{99} (≤2.6 Gy and 1.7 Gy, respectively). For large quality-of-life studies in which mean doses are summed up, such as the study by Teguh *et al.* (5), differences of this scale of magnitude are probably negligible. However, this approximation assumes modest deformations, which may not hold for other sites. Because of the low number of patients, these results should be interpreted with caution.

Apart from cases of head-and-neck cancer (10), our nonrigid registration framework has been used in other studies to analyze the deformation of the prostate and the seminal vesicles for prostate cancer patients (22) and for cervix cancer patients experiencing extreme deformations as a result of bladder filling variations (23). Based on this experience and the results described in this study, we expect our method for dose addition to be applicable to other sites treated with combined modality treatment (*e.g.,* prostate and gynecologic sites).

The method can also accumulate dose distributions from other radiation modalities. Dose accumulation can also be used to optimize radiation treatment plans that considering dose previously delivered to the patient (*e.g.,* optimizing BT plans taking the EBRT dose into account). Also, using a better total dose approximation, treatment-related toxicity and dose–effect relationships can be determined more accurately.

CONCLUSION

We have presented a reliable and robust method that allows adding 3D dose distributions of combined EBRT and BT for organs at risk in patients with oropharyngeal cancer. Further improvements, for example in areas with steep dose gradient, can be expected if structures inside the organs can be extracted in the images and used in the nonrigid registration. Optimization of BT plans while taking into account the EBRT dose already delivered, and replanning in adaptive strategies, are promising new possibilities.

REFERENCES

1. Levendag P, Nijdam W, Noever I, *et al*. Brachytherapy versus surgery in carcinoma of tonsillar fossa and/or soft palate: Late adverse sequelae and performance status: Can we be more selective and obtain better tissue sparing? *Int J Radiat Oncol Biol Phys* 2004;59:713–724.
2. Pearce A, Craighead P, Kay I, *et al*. Brachytherapy for carcinoma of the cervix: A Canadian survey of practice patterns in a changing era. *Radiother Oncol* 2009;91:194–196.
3. Zelefsky MJ, Nedelka MA, Arican ZL, *et al*. Combined brachytherapy with external beam radiotherapy for localized

prostate cancer: Reduced morbidity with an intraoperative brachytherapy planning technique and supplemental intensity-modulated radiation therapy. *Brachytherapy* 2008;7:1–6.
4. Ares C, Popowski Y, Pampallona S, *et al*. Hypofractionated boost with high-dose-rate brachytherapy and open magnetic resonance imaging-guided implants for locally aggressive prostate cancer: A sequential dose-escalation pilot study. *Int J Radiat Oncol Biol Phys* 2009;75:656–663.
5. Teguh DN, Levendag PC, Noever I, *et al*. Treatment techniques and site considerations regarding dysphagia-related quality of life in cancer of the oropharynx and nasopharynx. *Int J Radiat Oncol Biol Phys* 2008;72:1119–1127.
6. Steel GG, editor. Basic clinical radiobiology. London: Hodder Arnold; 2002.
7. Chui H, Rangarajan A. A new point matching algorithm for non-rigid registration. *Computer Vision and Image Understanding* 2003;89:114–141.
8. Vásquez Osorio EM, Hoogeman MS, Bondar L, *et al*. A novel flexible framework with automatic feature correspondence optimization for nonrigid registration in radiotherapy. *Med Phys* 2009;36:2848–2859.
9. Bondar L, Hoogeman MS, Vásquez Osorio EM, *et al*. A symmetric nonrigid registration method to handle large organ deformations in cervical cancer patients. *Med Phys* 2010;37: 3760–3772.
10. Vásquez Osorio EM, Hoogeman MS, Al-Mamgani A, *et al*. Local anatomic changes in parotid and submandibular glands during radiotherapy for oropharynx cancer and correlation with dose, studied in detail with nonrigid registration. *Int J Radiat Oncol Biol Phys* 2008;70:875–882.
11. Kolkman-Deurloo IK. Intraoperative HDR brachytherapy: Present and future [PhD thesis]. Rotterdam: Erasmus University; 2006.
12. Ibanez L, Schroeder W, Ng L, *et al*. The ITK software guide. New York: Kitware Inc; 2005.
13. Wendling M, Zijp LJ, McDermott LN, *et al*. A fast algorithm for gamma evaluation in 3D. *Med Phys* 2007;34:1647–1654.
14. Bookstein F. Principal warps: Thin-plate splines and the decomposition of deformations. *IEEE Trans Pattern Anal Mach Intell* 1989;11:567–585.
15. Fowler JF. Sensitivity analysis of parameters in linear-quadratic radiobiologic modeling. *Int J Radiat Oncol Biol Phys* 2009;73:1532–1537.
16. Rosu M, Chetty IJ, Balter JM, *et al*. Dose reconstruction in deforming lung anatomy: Dose grid size effects and clinical implications. *Med Phys* 2005;32:2487–2495.
17. Schaly B, Kempe JA, Bauman GS, *et al*. Tracking the dose distribution in radiation therapy by accounting for variable anatomy. *Phys Med Biol* 2004;49:791–805.
18. Brock KK, McShan DL, Ten Haken RK, *et al*. Inclusion of organ deformation in dose calculations. *Med Phys* 2003;30: 290–295.
19. Chi Y, Liang J, Yan D. A material sensitivity study on the accuracy of deformable organ registration using linear biomechanical models. *Med Phys* 2006;33:421–433.
20. Zhong H, Kim J, Chetty IJ. Analysis of deformable image registration accuracy using computational modeling. *Med Phys* 2010;37:970–979.
21. Robar JL, Day A, Clancey J, *et al*. Spatial and dosimetric variability of organs at risk in head-and-neck intensity-modulated radiotherapy. *Int J Radiat Oncol Biol Phys* 2007;68: 1121–1130.
22. van der Wielen GJ, Incrocci TFML, Kirkels WJ, *et al*. Deformation of the prostate and seminal vesicles relative to intraprostatic fiducial markers. *Int J Radiat Oncol Biol Phys* 2008;72:1604–1611.
23. Bondar M, Hoogeman M, Dhawtal G, *et al*. TU-D-BRC-06: Towards online image guided radiotherapy for cervical cancer: Accurate cervix-uterus prediction based on measured bladder volumes. *AAPM* 2009;36:2735. 2735.